

# Detecting and characterising returns in a pulsed lidar system

A.M. Wallace, R.C.W. Sung, G.S. Buller, R.D. Harkins, R.E. Warburton and R.A. Lamb

**Abstract:** A new multi-spectral laser radar (lidar) system based on the time-correlated single photon counting, time-of-flight technique has been designed to detect and characterise distributed targets at ranges of several kilometres. The system uses six separated laser channels in the visible and near infrared part of the electromagnetic spectrum. The authors present a method to detect the numbers, positions, heights and shape parameters of returns from this system, used for range profiling and target classification. The algorithm has two principal stages: non-parametric bump hunting based on an analysis of the smoothed derivatives of the photon count histogram in scale space, and maximum likelihood estimation using Poisson statistics. The approach is demonstrated on simulated and real data from a multi-spectral lidar system, showing that the return parameters can be estimated to a high degree of accuracy.

## 1 Introduction

Laser radar (lidar) is an established technique for 3D surface measurement in industrial or other commercial applications [1], for airborne scanning and mapping [2] and for the detection, ranging and recognition of remote targets in defence [3]. In the latter context, the lidar has the ability to acquire both reflectance and geometric data simultaneously from the target, thus providing potentially a more powerful classification tool than a purely passive source in the visible or infrared wavebands. To produce a full three-dimensional (3D) image [4], such lidars can be built either using a single detector with a scanning mechanism in two dimensions, a linear array of detectors with a scanning mechanism in one dimension or a focal plane array of either integrating sensor elements combined with a gated source (burst illumination, flash lidar) [5] or of 3D range sensing elements such as avalanche photodiodes [6] or PIN devices [7]. If a multi-spectral capability is included, that is, the ability to acquire images of the target at several different wavelengths [4, 7], then it is possible to combine the 3D geometry of the laser ranging with the spectral signature of the response to provide very informative data about the nature of the target.

To date, the majority of lidar systems have concentrated on the analysis of a single assumed return from an opaque surface normal to the beam to produce a range measurement, typically using pulsed, AM or FM signals [1]. In contrast, we have developed a time-of-flight (TOF) 3D imaging technique based on time-correlated single photon counting (TCSPC) [8, 9], capable of resolving returns from several

surface reflections. TCSPC is a statistical sampling technique which relies on the accumulation of a large number of individual measurements of photon return time in order to significantly improve the overall system accuracy. Typically, such systems use a picosecond duration pulsed source (usually a pulsed semiconductor laser) and a silicon-based single photon avalanche diode (SPAD) detector. These components can lead to a jitter of 100–500 ps in the return signal for a single photon measurement, but by accumulation of photon returns and post-processing of the histogram, a time resolution of lower than 1 ps has been demonstrated. Most of our previous work has been directed towards high accuracy scanning of uncooperative surfaces at short ranges, for example 20  $\mu\text{m}$  depth resolution at a distance of 2 m [8, 9], aimed primarily at applications in industrial metrology. However, we have also looked at the application of the technology to longer distances (10–100 m) for scanning of architectural and archaeological artefacts. For a description of the fundamental approach the reader is directed to [8].

In this paper, we discuss the processing of data from a new, static ground-based multi-spectral lidar system to acquire 3D data from targets at several kilometres. As in the previous work referred to in the opening paragraph, we combine the acquisition of 3D data with a multi-spectral capability, but there is an important difference in the TOF-TCSPC approach. Specifically, photon returns from a distant target can be accumulated from anywhere within the incident laser beam, for example from several transparent surfaces on the same axis, or from several opaque or transparent surfaces falling within the beam diameter. Our goal in the analysis of the TOF-TCSPC data is to determine the range and characteristic signature of remote targets, including the effects of distributed targets. If a single sensor (at each wavelength) is used, then we cannot reconstruct 3D geometry unless there is a scanning mechanism, but the geometry of the target is represented by a signature/histogram of the distribution of depths of the surfaces in the beam. Combining the target signatures at each wavelength is indicative of the range and spectral nature of the target. Although the acquisition of full 3D geometry requires a scan or a focal plane array, as noted above, the

© IEE, 2006

*IEE Proceedings* online no. 20045023

doi:10.1049/ip-vis:20045023

Paper first received 12th May 2004 and in final revised form 6th July 2005

A.M. Wallace, R.C.W. Sung, G.S. Buller, R.D. Harkins and R.E. Warburton are with the School of Engineering and Physical Sciences, Heriot-Watt University, Riccarton, Edinburgh EH14 4AS, UK

R.A. Lamb is with Qinetiq, St. Andrews Road, Malvern, Worcestershire WR14 3PS, UK

E-mail: a.m.wallace@hw.ac.uk

depth distribution of the surfaces is still very informative. For a single spectrum, we wish to determine

- the number of surface returns present,
- the amplitude of each of these returns,
- the position of each of these returns and
- the signal parameter vectors, when allowed to vary from a reference (instrumental) response.

## 2 Multi-spectral ranging system for distributed targets

The multi-spectral lidar system extends the basic principle of TCSPC-TOF described in [8] and elsewhere to multiple wavelengths in the visible and near infrared part of the spectrum, as illustrated in Fig. 1. The system is designed to operate at ranges of several kilometres, and has six transmitting laser diodes of wavelengths 630, 686, 780, 841, 911 and 975 nm arranged in a ring around a receiving Schmidt-Cassegrain telescope that focuses the broadband return onto an optical fibre mounted on a translation stage. The wavelengths are separated by an optical routing module into the six distinct narrowband channels, each of which is focused in turn on a channel-specific SPAD. The time multiplexing of the channels is performed by a multi-wavelength sequencer.

The trigger for a photon measurement comes from the laser driver, so that the SPAD (in each channel) records the arrival time of a detected photon. As the laser is pulsed repetitively, multiple photon events contribute to the formation of a histogram of photon events whose horizontal axis is time of arrival after the transmitted laser pulse, and vertical axis is the number of recorded events in each histogram bin. In contrast to other types of lidar system, the TCSPC approach is capable of greater sensitivity and accuracy of measurement, and is much less susceptible to range-intensity crosstalk or ‘random walks’ caused by varying reflectance and signal amplitude on the distance measurement. If the surface reflectance is reduced, then the number of photon counts is reduced (for a given collection time), but the distribution and method of analysis is unchanged. A discussion of the measurement accuracy as a function of the number of collected photons, whether changed by variation of collection time or reflectance, can be found in Pellegrini *et al.* [10]. A further common source of error in range measurement is due to temperature variation. The effect of this factor on photon count systems was reported by Massa *et al.* [9]. Range-intensity crosstalk and temperature variation have not

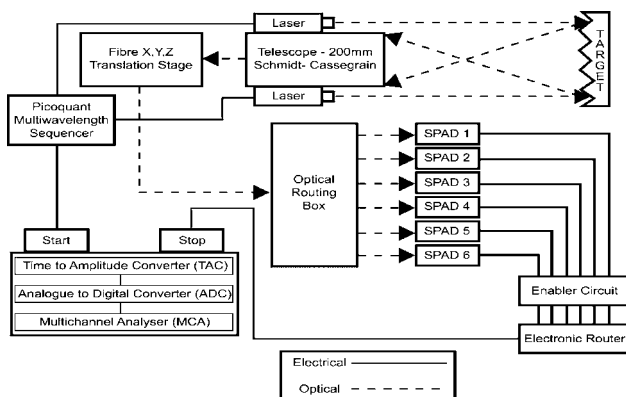


**Fig. 1** Schematic diagram of the multi-spectral, TCSPC-TOF system for target ranging and classification

been evaluated as systematically for the multi-spectral system, but we have varied collection time and used targets of very different reflectivity in the experiments presented here and the results are consistent with our previous observations.

For a single wavelength, we can analyse that distribution to find the distance to, and nature of, the target. However, differences between the wavelengths can also be used for target classification. Figs. 2a, c and d illustrate on a logarithmic scale some examples of data acquired by the multi-spectral system. Fig. 2a is a corner cube that can be used as an instrumental response. Figs. 2c and d are two examples from one of several test targets we used, a wavy metal plate shown in Fig. 8a. What are immediately apparent from Figs. 2c and 2d is that the shape of the histogram is quite different at the two wavelengths, and that the measured histogram does not come from a single normal surface. This forms an effective basis for both range measurement and target discrimination. Fig. 2b shows the fitting of the piecewise exponential (PE) function to the data from the corner cube; this defines the initial parameter set of (1) that is used to characterise the target signatures such as those shown in Figs. 2c and d.

## 3 Modelling the photon count data

Previously [11], we obtained accurate estimates of the peak position of a single return by iterative fitting of an operating model to either the raw histogram data or to the auto-correlation function and minimisation of an error metric. The exact functional form of the histogram was unknown, so we employed a nearest representation or operating model based on the product of a Lorentzian key function and the summation of Hermite polynomials to describe the underlying distribution. The best parameters for this operating model were determined by a maximum likelihood estimation (MLE) using the approximation that the true Poisson distribution of photon count data could be represented by a Gaussian distribution if the count levels are sufficiently large. This method was successful in recording an average localisation error of 0.1 ps in measuring the time separation of two peaks in the histogram, using a bin width of 2.44 ps. However, it was necessary to limit the time index of the photon counts (i.e. the width of the peak) as the higher order Hermite polynomials (like any polynomial) have oscillations of large magnitude at high index values [12]. If a histogram contains multiple responses of quite different magnitudes, the implementation of a step (or other) function truncation of a signal of high magnitude can obscure a genuine but much smaller response. Further, if the returns are low in amplitude, which may be due to increased range, shorter acquisition times or lower reflectance from the target, the Gaussian approximation may no longer be valid. Therefore, we employ the alternative of a set of four PE functions to model the histogram response of a single peak in this work

$$f(i, p) = \beta \begin{cases} e^{-(i-i_0)^2/2\sigma^2} e^{-(i-i_1)/\tau_1} & i < i_1 \\ e^{-(i-i_0)^2/2\sigma^2} & i_1 \leq i < i_2 \\ e^{-(i_2-i_0)^2/2\sigma^2} e^{-(i-i_2)/\tau_2} & i_2 \leq i < i_3 \\ e^{-(i_2-i_0)^2/2\sigma^2} e^{-(i_3-i_2)/\tau_2} e^{-(i-i_3)/\tau_3} & i \geq i_3 \end{cases} \quad (1)$$

The parameter set for a single return,  $p = \{\beta, \sigma, i_0, i_1, i_2, i_3, \tau_1, \tau_2, \tau_3\}$ . If desired, it is also possible to enforce first order

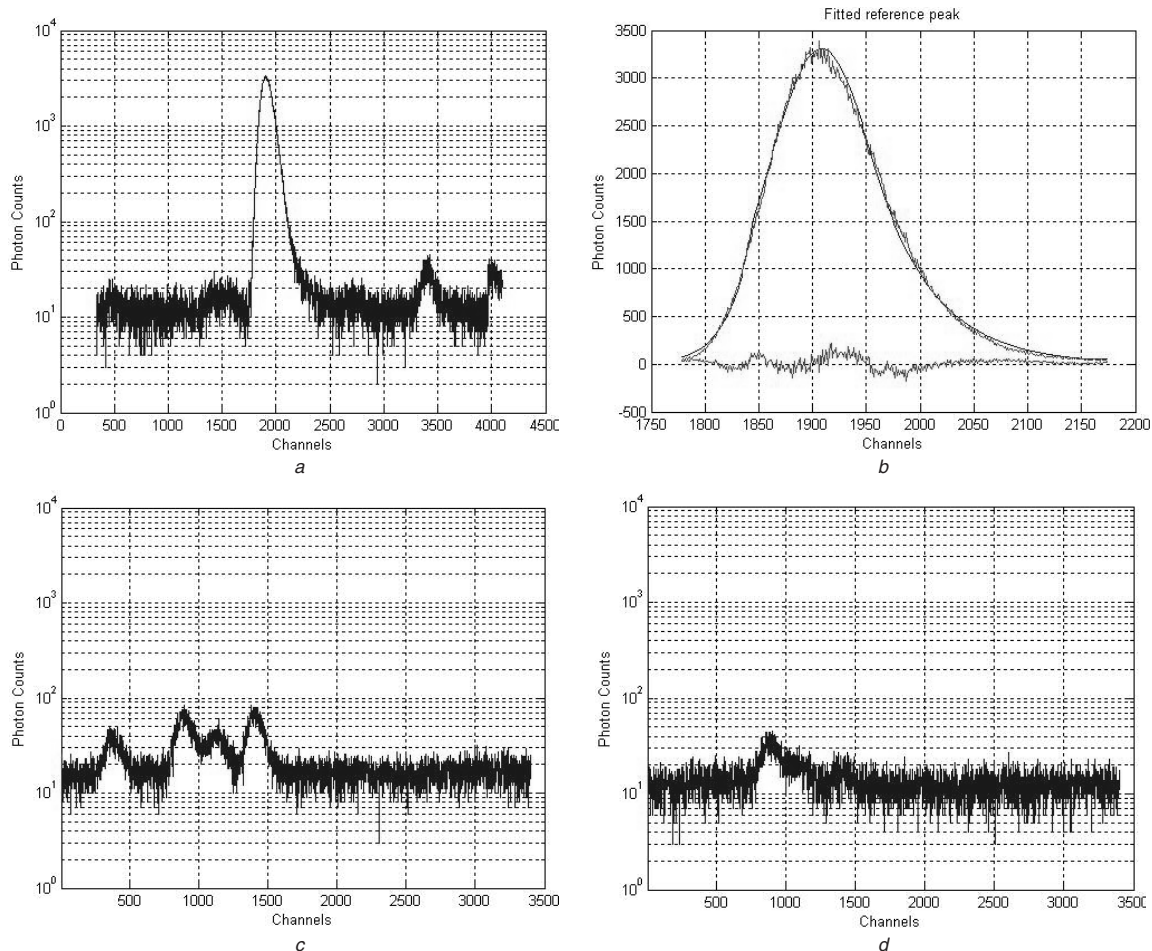


**Fig. 2** Examples of data acquired by the multi-spectral system

*a* Data from a corner cube at 330 m,  $\lambda = 630$  nm

*b* Fitting the PE function to the corner cube data

*c* Target data,  $\lambda = 630$  nm

*d* Target data,  $\lambda = 780$  nm

One bin (channel) corresponds to 6.1 ps

continuity (C1) constraints on the PE model so that the gradients at the transitions are also equal, that is

$$\begin{aligned} \sigma^2 + \tau_1(i_1 - i_0) &= 0 \quad \text{at } i_1 \\ \sigma^2 - \tau_2(i_2 - i_0) &= 0 \quad \text{at } i_2 \\ \tau_2 - \tau_3 &= 0 \quad \text{at } i_3 \end{aligned} \quad (2)$$

As an example, Fig. 2b shows the fit of the PE function to the return from the corner cube, which can be considered as an approximation to an instrumental response. Although the PE model is an operating model rather than a true model of the response of a SPAD, Stellari *et al.* [13] have observed in their studies of the temporal response of similar devices that the ‘SPAD response has a regular shape, with a Gaussian peak and an exponential tail’. For both our data and that of Stellari *et al.*, there is an apparent breakpoint in both the rising and falling part of the intrinsic time response that makes the four piecewise function a better model fit to the data.

In general, we wish to detect small, probably overlapping signals, observed against a finite background level that has a constant expected value across all channels in a single histogram, although that background level can vary as a function of integration time, temperature and wavelength. In that case, the function that defines the observed photon count

histogram,  $F(i, P)$ , is a statistical mixture constructed from a random sample of a distribution with density

$$F(i, P) = \sum_{j=1}^n f_j(i, p_j) + B \quad (3)$$

where  $n$  denotes the number of terms in the summation, which depends on the number of surface returns.  $f_j(i, p_j)$  denotes the functional form from the  $j$ th scatterer, where  $f(\cdot)$  is defined by (1). The parameter  $B$  represents the background photon count level. Assuming that the time resolution is sufficiently fine, the number of photons,  $c_i$ , in bin  $i$ , can be considered as a random sample from a Poisson distribution, with mean and variance  $F(i, P)$  that depends on the parameter set,  $P$

$$P(c_i) = e^{-F(i, P)} \frac{F(i, P)^{c_i}}{c_i!} \quad (4)$$

We have considered two forms of the parameter set,  $P$ , although other options are possible dependent on application. First, each return can have a distinct amplitude, shape and position. Hence,  $P = \{\beta_1, i_{01}, \dots, \tau_{31}, \dots, \beta_n, i_{0n}, \dots, \tau_{3n}, B\}$  and the parameter set has cardinality  $(9n + 1)$ . Second, the shape parameters are the same, and known from a prototypical or instrumental response.

Hence,  $P = \{\beta_1, is_1, \beta_2, is_2, \dots, \beta_n, is_n, B\}$ . This has cardinality  $(2n + 1)$ .

#### 4 Method: finding and characterising multiple peaks in the photon count data

We summarise a top-level description as Algorithm 1.

*Algorithm 1:*

Stage 1: Find putative signal positions in target data

- Set initial width for Gaussian smoothing kernel
- Repeat
  - Apply Gaussian kernels (Gaussian, first and second derivatives) to raw time series data
  - Compute diagnostic parameters on filtered data, for example, curvature, excess mass
  - Record positions and amplitudes of possible peaks on the basis of diagnostic measures
  - Reduce width of Gaussian kernel
- Until (maximum number of targets exceeded or minimum kernel width reached)
- Sort the  $k$ -peaks into descending order of peak height

Stage 2: Perform maximum likelihood estimation using variable numbers of peaks from Stage 1

- Assume initially a single peak is present
- Repeat
  - Perform maximum likelihood estimation using initial parameters of current list of putative peaks
  - Record value of resultant log-likelihood function
  - Add the next peak from the sorted list (\* with the option of adding further peaks at random)
- Until [the number of peaks from Stage 1 has been reached (\* or exceeded)]
- Record log-likelihood function, peak parameters and error measures for each number of peaks
- Determine the probable number, amplitudes and positions of peaks on this basis

To establish an initial, variable or fixed set of shape parameters (1), we use a corner cube or a ‘good’ external target as a reference. The photon spectrum may be shaped by multiple returns from semi-transparent surfaces, or from different surface depths within the illuminated area of the incident beam. If a target is distributed in depth within the field of view of the sensor, if the transmitted pulse profile or impulse response of the detector change or if the atmospheric conditions change, then the pulse profile is changed. Stage 1 is non-parametric, but in Stage 2 we estimate either  $(2n + 1)$  or  $(9n + 1)$  parameters, as defined in Section 3.

##### 4.1 Non-parametric peak finding in scale-space filtered data

The number of possible mixtures is combinatorially explosive, so we ‘bootstrap’ the analysis of the histogram by a bump hunting procedure [14] that provides an initial estimate of the number, amplitude and positions of the suspected returns. Depending on the amplitude and separation of discrete returns, a histogram of many returns may be multi-modal or multi-tangential (implied by multimodality). In noiseless data, it is simple to test for this by analysis of the differential structure of the data [15] but in noisy data such differential properties are amplified. We obtain a progressive series of kernel density estimates by linear filtering with Gaussian filters of progressively decreasing standard deviation,  $h$ . To interpret such data,

Silverman [16] tested the null hypothesis that a given kernel density estimate has  $k$ -modes against the alternative that it has less than  $k$ -modes. Chaudhuri and Marron [17] drew the analogy between kernel density estimates in statistics and scale-space filtering in computer vision to produce SiZer (Significant Zero crossings of derivatives) maps. Focusing on zero crossings of the derivative of the smoothed function, the SiZer map is a visual tool that shows the number of modes at each value of  $h$  in scale space. Fisher and Marron [18] later argued that critical bandwidth tests do not take into account the strength of the mode and included additional thresholds on both the height and excess mass of a mode.

In our approach, the original histogram is also smoothed by Gaussian and Gaussian derivative filters to detect structure, that is, progressively defined by the functions,  $G(i, h) = [1/\sqrt{(2\pi)h}]e^{-i^2/2h^2}$ ,  $G'(i, h) = [i/\sqrt{(2\pi)h^3}]e^{-i^2/2h^2}$ ,  $G''(i, h) = [(i^2/h^2 - 1)/\sqrt{(2\pi)h^3}]e^{-i^2/2h^2}$ . However, we focus on the curvature, that is, peaks in the second derivative, rather than zero crossings in the first derivative [17]. This arises primarily from the desire to detect multiple returns when indicated only by multi-tangentiality, for example in Fig. 4, where zero crossings do not exist in the first derivative Gaussian filtered data. To illustrate our approach, consider the analysis of the detection of a single mode in a photon count histogram by analysis of the smoothed second derivative. Using the Heaviside function,  $U(\cdot)$ , we can compute the convolved output of the PE function with the smoothed second derivative filter as

$$s(i, h, P) = \sum_{l=i-W}^{i+W} \begin{bmatrix} f_a(i, P) - f_a(i, P)U(i - i_1) \\ +f_b(i, P)U(i - i_1) - f_b(i, P)U(i - i_2) \\ +f_c(i, P)U(i - i_2) - f_c(i, P)U(i - i_3) \\ +f_d(i, P)U(i - i_3) + B \end{bmatrix} \times G''(i - l, h) \quad (5)$$

where  $f_{a-d}(i, P)$  are the four piecewise functions of (1) in temporal order. We use the function  $G''(i - l, h)$  for  $l > i + h$  and  $l < i - h$  and the inverse  $-G''(i - l, h) = 1/\sqrt{(2\pi)h^3}(1 - (i - l)^2/h^2)e^{-(i - l)^2/2h^2}$  for  $i - h < l < i + h$ . Splitting the convolution in this way, each discrete sum can be considered as a sum of Poisson distributed variables. Hence, the results are also Poisson distributed with means  $\mu_1$  and  $\mu_2$ . However, each entry in the convolved  $s(i, h, P)$  is a discrete spectrum in which each entry is the difference of these two Poisson distributed variables. The resulting probability distribution at each bin,  $i$ , is

$$P(c_i) = e^{-(\mu_1 + \mu_2)} \left( \frac{\mu_1}{\mu_2} \right)^{c_i/2} I_{c_i}(2\sqrt{\mu_1\mu_2}) \quad (6)$$

where  $\mu_1$  and  $\mu_2$  are the respective means and  $I(\cdot)$  is a modified Bessel function of the first kind [19]. The problem is to set a threshold to detect the presence of single or multiple pulses against a constant background, or against the background formed by other overlapping pulses. For clarity, consider the case where there is a single return and the width of the second differential filter function is contained wholly within the peak region of  $f(i, P)$ . This is useful because that is where we would expect the peak in the filtered signal. The approximation of the adjoining filter functions by the central Gaussian should not have a significant effect even if the window is slightly wider than the limits of the response because the count rates and filter coefficients are much lower. Further, the difference between the adjoining exponentials  $f_a(i, P)$ ,

$f_c(i, P)$  and the central Gaussian  $f_b(i, P)$  only deviates far from the breakpoints  $i_1$  and  $i_2$ . Then, from (1) and (5) we have

$$\begin{aligned} s(i, h, P) &= \sum_{l=i-W}^{i+W} f(l, P)G''(i-l, h) \\ &= \sum_{l=i-W}^{i+W} \left( \beta e^{-(l-i_0)^2/2\sigma^2} + B \right) \frac{1}{\sqrt{2\pi h^3}} \\ &\quad \times \left( \frac{(i-l)^2}{h^2} - 1 \right) e^{-(i-l)^2/2h^2} \end{aligned} \quad (7)$$

in the presence of a return, and

$$s(i, h, P) = \sum_{l=i-W}^{i+W} B \frac{1}{\sqrt{2\pi h^3}} \left( \frac{(i-l)^2}{h^2} - 1 \right) e^{-(i-l)^2/2h^2} \quad (8)$$

if no return is present. Hence, we can compute the mean levels,  $\mu_1$  and  $\mu_2$  of (6), for the two Poisson distributed components in bin  $i$  of the distribution of filtered photon count data when the maximum of the Gaussian filter coincides with the maximum of the PE of a return at position  $i_0$ . If a return is present, then the expected levels of the two means are found by splitting the convolution of (7) into the central and outer components of the discrete summation, as shown in (9)

$$\begin{aligned} \mu_1 &= \frac{1}{\sqrt{2\pi h^3}} \sum_{l=i_0-h}^{i_0+h} \left( 1 - \frac{(i_0-l)^2}{h^2} \right) \\ &\quad \times \left( \beta e^{-((l-i_0)^2/2\sigma^2 + (i_0-l)^2/2h^2)} + B e^{-(i_0-l)^2/2h^2} \right) \\ \mu_2 &= \frac{1}{\sqrt{2\pi h^3}} \sum_{l=-W}^{i_0-h} \left( \frac{(i_0-l)^2}{h^2} - 1 \right) \\ &\quad \times \left( \beta e^{-((l-i_0)^2/2\sigma^2 + (i_0-l)^2/2h^2)} + B e^{-(i_0-l)^2/2h^2} \right) \\ &\quad + \frac{1}{\sqrt{2\pi h^3}} \sum_{l=i_0+h}^W \left( \frac{(i_0-l)^2}{h^2} - 1 \right) \\ &\quad \times \left( \beta e^{-((l-i_0)^2/2\sigma^2 + (i_0-l)^2/2h^2)} + B e^{-(i_0-l)^2/2h^2} \right) \end{aligned} \quad (9)$$

In the absence of a return, (8) is split similarly into the two components to give

$$\begin{aligned} \mu_1 &= \frac{1}{\sqrt{2\pi h^3}} \sum_{l=i_0-h}^{i_0+h} B \left( 1 - \frac{(i_0-l)^2}{h^2} \right) e^{-(i_0-l)^2/2h^2} \\ \mu_2 &= \frac{1}{\sqrt{2\pi h^3}} \sum_{l=-W}^{i_0-h} B \left( \frac{(i_0-l)^2}{h^2} - 1 \right) e^{-(i_0-l)^2/2h^2} \\ &\quad + \frac{1}{\sqrt{2\pi h^3}} \sum_{l=i_0+h}^W B \left( \frac{(i_0-l)^2}{h^2} - 1 \right) e^{-(i_0-l)^2/2h^2} \end{aligned} \quad (10)$$

A minimum probability of error receiver is applied to the filtered data to detect the presence or absence of a return. Define the probability distribution of a signal in the presence and absence of a signal as  $f(c_i|H_1)$  and  $f(c_i|H_0)$ , respectively, where  $H_1$  and  $H_0$  denote the hypotheses that a return is present and absent. Further, we define the *a priori* probabilities of a return or no return as  $P_1$  and  $P_0$ , respectively, and the cost functions  $C_{ij}$  as the cost of a decision  $i$  given that the true hypothesis is  $j$ , then the

Bayes decision rule is

$$\begin{aligned} \Lambda(c_i) &= \frac{f(c_i|H_1)}{f(c_i|H_0)} = e^{-(\mu_{11} + \mu_{21} - \mu_{10} - \mu_{20})} \left( \frac{\mu_{11}\mu_{20}}{\mu_{21}\mu_{10}} \right)^{c_i/2} \\ &\quad \times \left( \frac{I_{c_i}(2\sqrt{\mu_{11}\mu_{21}})}{I_{c_i}(2\sqrt{\mu_{10}\mu_{20}})} \right) \stackrel{H_1}{\geq} \frac{P_0(C_{10} - C_{00})}{P_1(C_{01} - C_{11})} = \eta \end{aligned} \quad (11)$$

using the notation  $\mu_{ij}$  to denote mean  $i$  under hypothesis  $j$ .  $\eta$  is the threshold on the likelihood statistic,  $\Lambda(c_i)$ . For the minimum probability of error, the cost of an error ( $C_{01}$ ,  $C_{10}$ ) is normally 1, and of a correct decision ( $C_{11}$ ,  $C_{00}$ ) is 0, so that the right-hand side of (11) reduces to  $P_0/P_1$ . The error function is  $P_\varepsilon = P_M P_1 + P_F P_0$  where  $P_M$  and  $P_F$  are the probabilities of a missed target and false alarm, respectively. Taking natural logs, (11) can be re-arranged to give a quadratic in  $c_i$ . Finding the root of this quadratic allows us to set the threshold for the detection of the presence or absence of a pulse, where  $\eta$  is the ratio of *a priori* probabilities

$$\begin{aligned} \frac{c_i}{2} \ln \left( \frac{\mu_{11}\mu_{20}}{\mu_{21}\mu_{10}} \right) + \ln \left( \frac{I_{c_i}(2\sqrt{\mu_{11}\mu_{21}})}{I_{c_i}(2\sqrt{\mu_{10}\mu_{20}})} \right) \\ + (\mu_{10} + \mu_{20} - \mu_{11} - \mu_{21}) - \ln \eta \stackrel{H_1}{\geq} 0 \end{aligned} \quad (12)$$

A similar analysis for the Gaussian noise case gives the more familiar expression

$$\begin{aligned} c_i^2 \left( \frac{\sigma_1^2 - \sigma_2^2}{2\sigma_1^2\sigma_2^2} \right) + c_i \frac{(m_1\sigma_2^2 - m_2\sigma_1^2)}{\sigma_1^2\sigma_2^2} + \frac{(m_2^2\sigma_2^2 - m_1^2\sigma_1^2)}{2\sigma_1^2\sigma_2^2} \\ + \ln \left( \frac{\sigma_2}{\sigma_1} \right) - \ln \eta \stackrel{H_1}{\geq} 0 \end{aligned} \quad (13)$$

where  $m_1$ ,  $m_2$ ,  $\sigma_1$  and  $\sigma_2$  are the respective means and standard deviations.

Fig. 3a shows an example of a simulation of a return, based on a fit to real data parameters, in which  $\beta = B = 2$  counts, and  $i_0 = 1000$  bins. Looking at Fig. 3b, there is no significant difference between the expected distribution of the second Gaussian derivative filtered data using the true Poisson and a Gaussian noise assumption. In interpreting this data, it should be noted that the Gaussian filter coefficients have been normalised in (9) and (10). Therefore the Poisson distribution, although discrete, is not represented at integer values; the un-normalised, integrated count difference and sum peaks are at 0 and 45 counts, respectively, explaining why there is little difference between the Poisson and Gaussian distributions in this case. The decision functions in Fig. 3c, that is, (11) and (13), do diverge but the root in each case is at a normalised count level of 0.337. Fig. 3d shows that the effect of setting such a threshold in the particular example of Fig. 3a would give the true positive, but also a false positive between 600 and 700 bins. The possibility of false detection is small but non-zero, as illustrated in the curve for  $\beta = 2$  in Fig. 3e. The final three figures show the fitted, true peak from the MLE (discussed in the next section, the false peak is rejected as unlikely at this stage), and the effect of variation of the smoothing filter width on the probability of detection and of a false alarm assuming the threshold is set correctly. As expected, the performance improves rapidly as the width of the smoothing filter is matched to the anticipated shape of the histogram response, but there is no clear minimum as the filter width increases further.

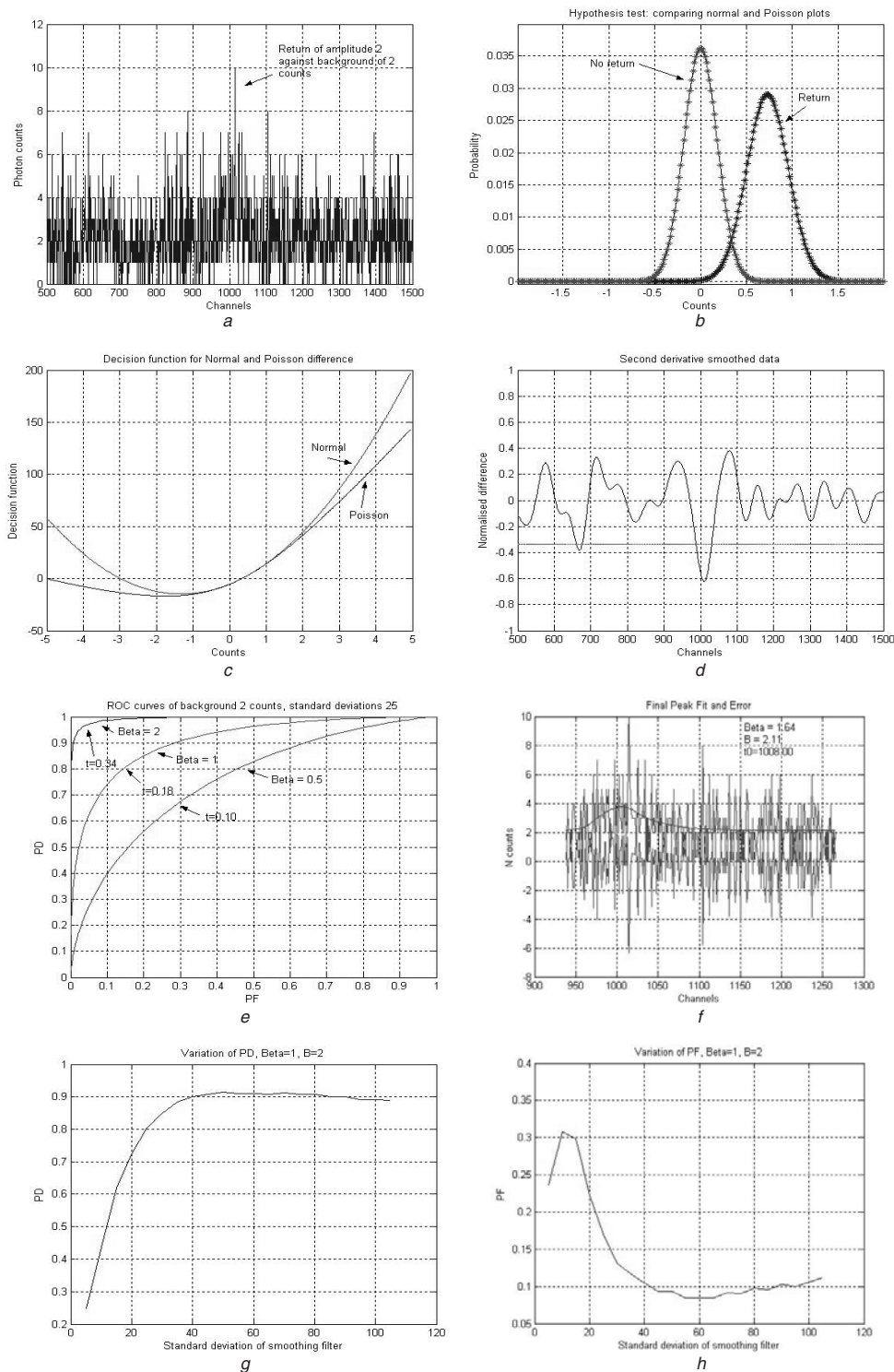


**Fig. 3** Example of a simulated signal

- a Example of a simulated signal of height two counts against a background level of two counts. The standard deviation of the peak exponential is 25.7 bins
- b Comparing the theoretical distributions of the curvature data for normal (solid line) and Poisson (crosses) distributions for a return of height two against a background of height two counts
- c Plotting (12) and (13) to decide the decision threshold, 0.337 in this case ( $\eta = 1$ )
- d Setting the decision threshold for curvature data; note the false alarm between 600 and 700 bins in this example
- e Theoretical receiver operating characteristic (ROC) curves for expected signal return heights of 2, 1 and 0.5 counts
- f The final fit from the ML estimation
- g Variation of probability of detection as a function of smoothing filter width
- h Variation of probability of a false alarm as a function of smoothing filter width

Fig. 4a shows a simulation of four returns present against a constant background level of five counts; the signal amplitudes are 50, 100, 45 and 50 counts at peak positions of 1884, 1935, 1990 and 2200 bins, respectively. This shows that multiple returns may not result in multiple modes. As

this is a simulation, the ground truth is known, so we can determine whether the bump hunting process on the smoothed derivatives can detect these peaks. Examining the smoothed first derivative ( $h = 12$  bins) in Fig. 4b, there is a clear zero crossing for each of the dominant

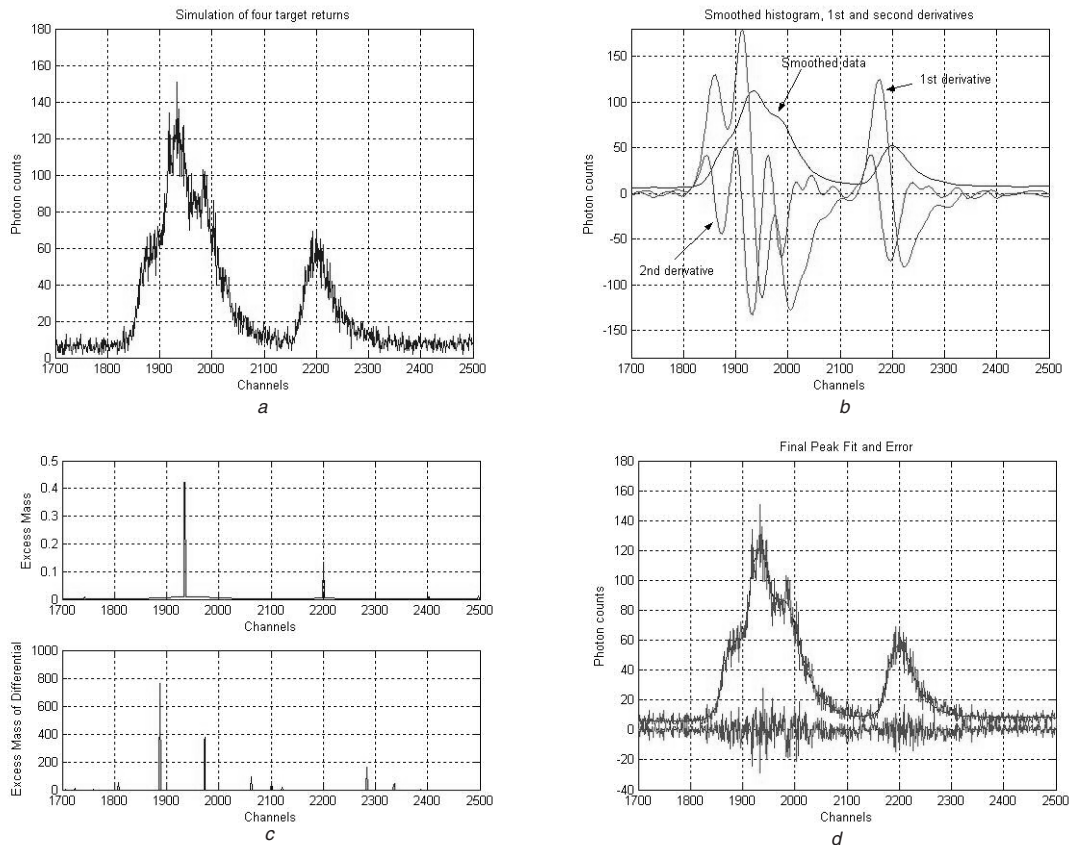


**Fig. 4** Simulated example of four closely spaced returns in a photon count histogram

- a Original histogram
- b Smoothed histogram, first and second derivatives
- c Excess mass in smoothed and smoothed derivative data
- d Final fit of four returns to simulated four peak data

peaks at 1935 and 2200 bins, but not at 1884 or 1990 bins. The second derivative data shows corresponding negative peaks at 1935 and 2200 bins and is equally effective, but the key advantage is in highlighting the co-tangential points at 1884 and 1990 bins. Where the first derivative is positive, the existence of a further negative peak in the curvature shows a possible additional return (1884 bins). Conversely, where the first derivative is negative, the existence of a further positive peak in the curvature shows a possible additional return (1990 bins). The excess mass estimate can also be used as a discriminant, defined as ‘the amount of mass that has to be shifted to convert a bimodal distribution into a unimodal distribution’ [18] and computed by measuring the number of counts in a mode in excess of both nearest local minima on either side of the peak. These are displayed in the upper panel of Fig. 4c, as a fraction of the total number of counts in the histogram. The co-tangents give an excess mass estimate of zero, and would not be detected by this method. Applied to the differential data of Fig. 4b, using positive or negative peaks to compute the excess mass as appropriate, the two largest masses are due to the two co-tangential returns.

#### 4.2 MLE of the parameters of the target

The addition of extra components will result generally in a closer fit, so that the most sensible approach is to assess the smallest number of components in the assumed mixture compatible with the data [20]. The bump hunting process gives only an initial estimate of the number and position

of returns. To refine that estimate, we define the MLE to find the set of parameters  $P$ , so that the function

$$L(c|P) = \prod_{i=1}^N \frac{F(i, P)^{c_i} e^{-F(i, P)}}{c_i!} \quad (14)$$

is maximised. As negative counts are not possible, and the product term is typically very small for any significant number of bins, it is more common to use the logarithm of this expression as minimising  $-2 \ln L(c|P)$  leads to the same parameters as maximising  $L(c|P)$ . The final term,  $\ln(c_i!)$ , is constant and can be omitted

$$-2 \ln L(c|P) = 2 \sum_{i=1}^N [F(i, P) - c_i \ln F(i, P)] \quad (15)$$

This expression has been used on a number of occasions to interpret photon count data [21, 22]. For example, Hannam and Thompson [21] compared MLE using Poisson statistics with least squares analysis and Gaussian statistics, in the latter case allowing for the dependence of the count variance on the mean, showing that the correct use of the Poisson statistics produced an improved estimate. If there are few fitting parameters, then it may be possible to find the MLE by setting expressions for each parameter derivative to zero [23] and finding the roots to these equations. However, in this work we have in general a function of  $(2n + 1)$  or  $(9n + 1)$  parameters and have applied constrained non-linear optimisation using sequential quadratic programming to find the MLE estimate. To justify this decision, the objective function must have a well-defined

minimum in the region of the initial estimates of the positions and heights of the returns derived in Stage 1. The initial estimate of the background level,  $B$ , comes from a region of the spectrum where the mean count level is constant. The initial estimates of the shape parameters (were allowed to vary), come from the fit to the reference of other instrumental signals. Then, the constraints employed in the optimisation process are:

- *Shape parameter vector*: all parameters are positive, since negative values are not physically realisable.
- *Breakpoint ordering*:  $i_1 < i_0 < i_2 < i_3$  as that corresponds to the piecewise definition of (1).
- *Width constraint*: a multiplicative constraint is placed on variation of the function width.
- *Amplitude constraint*: a multiplicative constraint is placed on variation of the function height.
- *Gradient constraints*: C1 continuity may be enforced as defined by (2).

In general, the addition of more returns (and parameters) will result in a better fit to the data. We do not define an absolute threshold on the log-likelihood function, rather the log-likelihood function should decrease rapidly then remain approximately constant when the optimum interpretation of the number of returns is reached, and we use this likelihood here to assess the probable number of signal returns. The problem with the likelihood is that it does not correct for the model complexity, unlike the Akaike ( $AIC = -2 \log[L(c|\hat{P}) + 2\kappa]$ ), Bayesian ( $BIC = -2 \log[L(c|\hat{P}) + \log(N)\kappa]$ ) information and minimum distance length ( $MDL = -2 \log[L(c|\hat{P}) + (1/2) \log(N)\kappa]$ ) criteria, each of which adds a penalty to the MLE based on the number of free parameters,  $\kappa$  [24].

Fig. 4d and Table 1 show the final result of the ML estimate of the number and position of returns in our simulated example. A fifth peak was found in Stage 1 but this was rejected by the subsequent estimation. It should be noted that the progressive decrease of the log-likelihood function is dependent on the order of fit. In this case, there is a large decrease on addition of the fourth peak because this is the separated mode at 2200 bins. The broadening of the main peak ( $\sigma = 47.87$  against 21.37 in the reference) is another major factor, showing the ill-posed nature of the problem as discussed earlier. Allowing the peak to broaden affects the estimated amplitudes and

positions of the multiple peaks. We explore these concerns further in the next section.

## 5 Experimental evaluation

In this section, we present results on both simulated and real data. To evaluate the bump hunting process we have performed extensive simulations of peak detection for a range of signal-to-background ratios (SBR), comparing the probabilities of true and false peak detection with the theory of Section 4, and also comparing the results against a standard non-negative least squares (NNLSQ) algorithm that assumes Gaussian statistics. We also present results for MLE to compare the results of parameter estimation with known ground truth when multiple returns are simulated from real spectral signatures. For real data, we have evaluated the ability of the system to measure target separation at long range, using corner cubes mounted on a ruled gauge to give an accurate comparison. Further, we characterise the real spectral signatures in different channels from multiple targets of varying surface reflectivity to show how the process can determine both range and spectral profiles.

### 5.1 Simulated data: evaluation of the bump hunting process to detect single and double returns

We have assessed the sensitivity of the bump hunting process to the curvature statistic used to detect single peaks, and compared it to detection by thresholding the response from NNLSQ [25], that is, minimising  $|A(P) \cdot s - f(i, P)|^2$ , where the impulse response,  $A(P)$ , is known and  $s$  is a source signal consisting of a perfect impulse scatterer. A real data sample was used to model the shape of the simulated response, as before, and this was then placed at an arbitrary location, bin number 1000. To assess the detection of false peaks the same process is applied, but the simulated data has no peak, that is, it is just a constant background signal with Poisson variations. The experiment was performed for a single peak at three values of the peak to background level, as shown in Fig. 5.

At higher signal-to-background levels, the probability of false classification decreases markedly, so these curves are not shown. The data points in Fig. 5 are the results of 50 trials in each case with the excess mass threshold set to

**Table 1: Illustrative results from simulations of Fig. 4**

Parameters	Reference	First peak	Second peak	Third peak	Fourth peak
$\beta$ (counts)	540.03	95.61 (100)	69.65 (45)	38.91 (50)	48.35 (50)
$\sigma$ (bins)	21.37	47.87	28.82	26.90	24.45
$t_0$ (bins)	2298.21	1937.79 (1935)	1984.86 (1990)	1879.32 (1884)	2201.19 (2200)
$t_1$ (bins)	2275.26	1884.54	1971.99	1862.88	2175.47
$t_2$ (bins)	2310.67	1944.02	2011.69	1889.97	2218.02
$t_3$ (bins)	2404.95	2067.23	2043.09	2011.59	2333.23
$\tau_1$ (bins)	12.20	24.24	24.40	10.21	8.34
$\tau_2$ (bins)	36.77	18.38	39.01	18.38	29.17
$\tau_3$ (bins)	604.96	590.38	302.47	603.53	599.10
$-2 \ln L(c P)$	No peaks - 106006	First peak - 142888	Second peak - 143022	Third peak - 143218	Fourth peak - 146338

Real data from the multi-spectral sensor was used as a model for the histogram distribution. The upper part of the table shows the final values of the three parameters, allowing all parameters to vary. The lower part shows  $-2 \ln L(c|P)$  to the nearest integer. The true simulated peak heights and positions are shown in brackets. The computed background level was 5.92 (5) counts

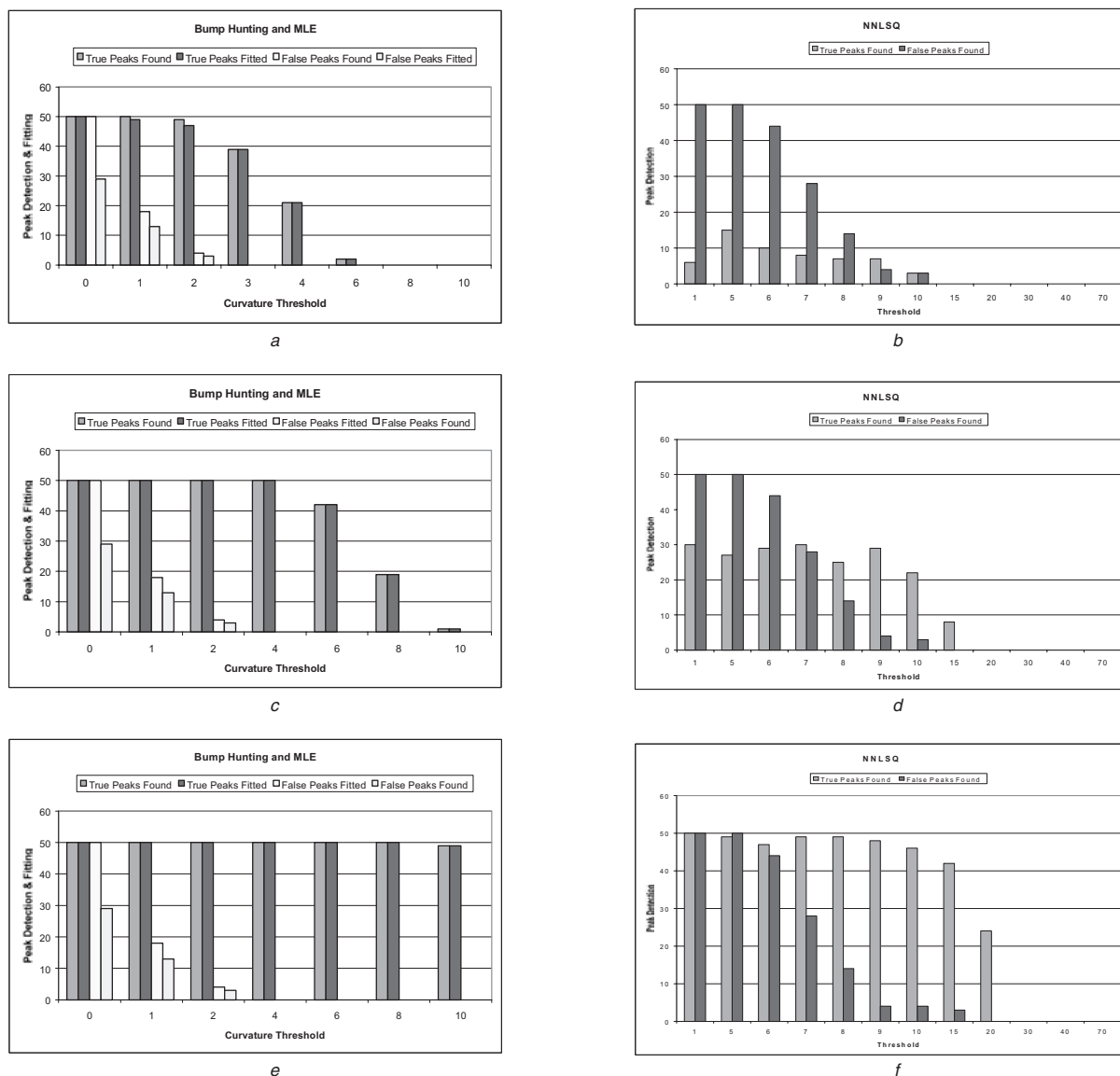


**Fig. 5** Comparing the use of the scale space curvature threshold (on the left) to the NNLSQ approach (on the right) From top to bottom, the peak heights are 2.5, 5 and 10 counts against a background of five counts. On the left, the four columns show true peaks found, true peaks fitted, false peaks found and false peaks fitted, respectively

zero, that is, the curvature alone is used as a threshold. In each figure, the threshold is increased progressively from left to right, so that the number of false positives should decrease, but true positives should also decrease. This does not happen monotonically due to the random nature of the trials. In general, the curvature statistic gives a better measure of the presence or absence of a mode, as is most evident from the  $SBR = 2.5 : 5$  data. For example, the left figure shows that at a curvature threshold of 2, 49 of the 50 true peaks are found and 47 fitted, but there are only four false positives of which three are fitted. If we look at the corresponding NNLSQ data, then the best result is probably at a threshold of nine, that is, the only one where the true peaks total of seven exceeds the false peaks total of four. Another comparison can be made between the results of the theoretical analysis in Fig. 3 that show an optimum probability of true detection of about 0.8 against a probability of false detection of 0.14 at an optimum threshold. In fact, the results of the simulation presented here are better than those predicted in Fig. 3, although neither the thresholds nor the detection of true and false peaks are directly comparable. In particular, the analysis of Fig. 3 includes only the central portion of

the peak, so this results in a difference between the ROC values.

### 5.2 MLE and the variation of the objective function

The next experiments were designed to compare the use of the full Poisson likelihood model against the least squares approximation, but constraining the predicted number of counts to be non-negative, as this results in major errors [21]. We ran simulations at various values of peak height, position and background level to measure the variation of the extracted parameters. As expected, there was no appreciable difference in the estimated parameters when the signal and background levels were high, but we anticipated that when the signal and background levels were low, the true Poissonian model would give statistically better estimates of the position, signal and background levels. Fig. 6 is typical and shows some examples for the estimation of signal and background heights on sets of 500 simulations of a return of mean amplitude 1.000 counts. Figs. 6a and b show histograms of the results

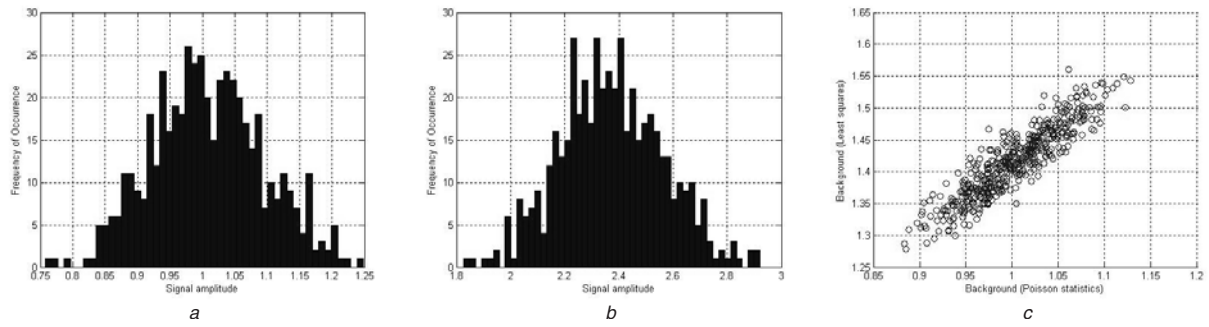


**Fig. 6** *Estimated height from 500 trials*  
 a Poisson statistics  
 b Gaussian statistics  
 c Comparison of the two estimates

when no background is present; as expected, the use of the Poisson-MLE gives an excellent estimate of 1.008 counts, whereas the least squares estimate is 2.373 counts. Fig. 6c shows a scatter-plot of the estimates of the background level when a constant photon count of 1.000 counts is added to the signal. Again, the Poisson-MLE estimate, 1.022 counts, is close to the true value, but the least squares process gives an over-estimate of 1.416 counts, when the signal amplitude is correctly constrained. This latter result is very close to the asymptotic mean estimate of  $\mu\sqrt{[1 + (1/\mu)]} = \sqrt{2}$  derived and tested in [22, 23]. In this, as in other examples, there is a high correlation (coefficient = 0.91) between the two estimates, as the random simulation is a dominant factor.

In the next experiment, we wanted to examine by simulation, the resolution of the peak estimation process for larger returns, that is, to determine the minimum separation of returns that could be both found and fitted by the system. Therefore in Fig. 7a we show the result of the measured separation of two returns of known height, 2000 counts, with a background level of five counts against the true values known from the simulation parameters. As can be seen, the measured and actual separations correspond well above 16 bins, but below this point even the bitangents become difficult to detect and the initial estimate of the peak separation is too unreliable to successfully complete the MLE process. In Fig. 7b, the peak separation is kept constant at 128 bins, but the ratio of peak heights is varied from 1 : 1, that is, each peak of height 2000 counts, to 16 : 1, that is, the minor peak has height 125 counts.

The figure shows the measured against the true peak separation and gives a maximum error of about 8%.

### 5.3 Processing real data

We have run several trials on the data acquired using the multi-spectral system. Fig. 8 shows an example of some test objects we used to collect ladar data in one trial, that we designate as ‘horn’, ‘wavy plate’, ‘truck’ and ‘sphinx’, from left to right in the picture. Although toys, these objects were chosen because of their shape and different responses at different wavelengths. As the range was relatively short, the angle subtended by these test objects was roughly equivalent to vehicles at longer ranges, although the atmospheric path is of course less of a problem. However, we also used corner cubes to perform systematic distance resolution trials and to provide a clean instrumental response, as shown for example in Fig. 2a.

We illustrate in Fig. 9, the response of the system to the wavy plate, which has lateral dimensions of approximately 15 cm by 40 cm, in the spectral channels at 630 and 780 nm. The subsidiary peak shown between 800 and 1000 bins in Fig. 9a is from the support, not the plate; the plate data is between 1200 and 1900 bins approximately. In this experiment, performed in the evening, in conditions similar to those illustrated in Fig. 8, we pulsed the laser at 20 MHz for a relatively long collection time of 30 s when the plate was situated at a distance of 330 m from the ladar system. At that distance, the beam width was approximately 33 cm as the divergence is of the order of 1 mrad. As an

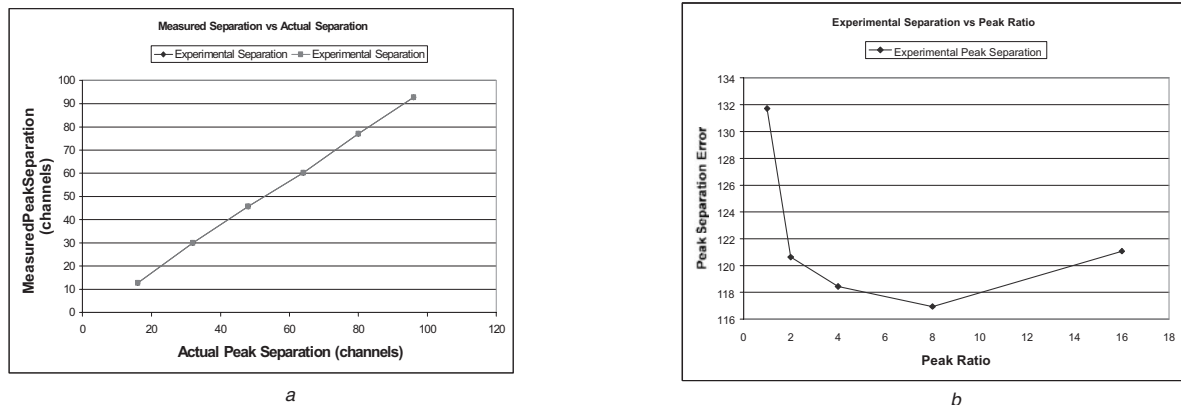


**Fig. 7** *Measuring the return resolution of the MLE process*  
 a Variation of measured against true peak separation for two peaks of height 2000 counts  
 b Measured peak separation for two peaks as a function of peak height ratio, two peaks separated by 128 bins

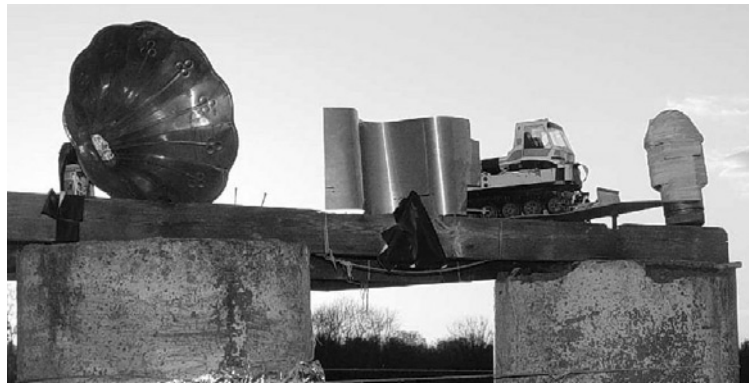


**Fig. 8** Examples of test objects used to assess the performance of the multi-spectral lidar system

instrumental response, we used data from a corner cube in the same spectral channels. In the data shown, we fixed the parameter vector,  $p = \{\beta, \sigma, i_0, i_1, i_2, i_3, \tau_1, \tau_2, \tau_3\}$ , of (1) from the fitted response to the corner cube data, that is, we sought to find the amplitudes and positions of the multiple returns, and the background level in each channel. The first observation is that there is considerable difference between Figs. 9a and 9b, showing that it is possible to determine information about the spectral response of the surface by using more than one channel. The second observation is that each channel has multiple peaks. In the 630 nm channel, the respective [position (bins), amplitude (counts)] values are {1900.55, 50.72}, {1389.35, 51.85}, {1619.37, 25.15} and {871.92, 22.43}. The background level is 16.22. In the 780 nm channel, the corresponding values are {1378.23, 25.55}, {1576.30, 10.51} {1890.57, 8.12}. The background level is 11.27. In this experiment, 1 bin corresponded to 6.1 ps. Fig. 9 shows both the original photon count data and the smooth parametric function of (3). The lowest data in each graph is the error between the smooth parametric curve and the original noisy data.

The next example, in Fig. 10, is somewhat different. In this case, we used the horn, but the beam was reflected back towards the optical telescope from the interior surface distributed in depth with respect to the viewer. We are not able to detect multiple modes in either the original or Gaussian filtered data because the effect of the distributed surface is to broaden the response, as can be seen clearly when we compare the upper curve of Fig. 10a, from the horn, to the reference corner cube data, the lower curve. In this case, we cannot obtain a good fit of the un-modified

parametric function to the horn data. However, we can allow the parameter vector to vary and obtain an optimum response with respect to all the parameters of (1), not just the amplitude and position. For comparison, for the corner cube,  $p$  is  $\{\beta = 2363.54, \sigma = 50.88, i_0 = 2016.53, i_1 = 1952.92, i_2 = 2062.86, i_3 = 2256.90, \tau_1 = 22.07, \tau_2 = 53.98, \tau_3 = 1079.68\}$  but for the horn,  $p$  is  $\{\beta = 1.587.09, \sigma = 74.39, i_0 = 2023.33, i_1 = 1897.98, i_2 = 2081.32, i_3 = 2234.44, \tau_1 = 44.15, \tau_2 = 95.45, \tau_3 = 1076.18\}$ . The clearest indication of the broadening of the peak is probably a comparison of the  $\sigma$  values, showing the wider standard deviation of the central Gaussian response for the horn.

We have also tested the range resolution of the system using a pair of reflecting corner cubes at mean distances of 330 m and 2 km at collection times of 0.1, 1 and 10 s to show the measured against the true separation of the two peaks for real data. We varied the separation of the corner cubes by small increments in distance that could be measured accurately by a ruled gauge to an accuracy of 1 mm. In general, provided the two peaks are well separated and give two modes in the histogram then the peaks are detected automatically and the separation of the fitted peaks gives a measure in bins that can be compared to the true separation. For example, Fig. 11a shows a result for a separation of 9.37 cm at a distance of 330 m. The histogram gives two distinct modes, although there is overlap between the responses. Fig. 11b shows a graph of the distance measured by the 630 nm channel of the multi-spectral system against 'ground truth' measured by a ruled gauge to an accuracy of 1 mm, as the separation was varied from 2 cm to 24 cm. A regression fit

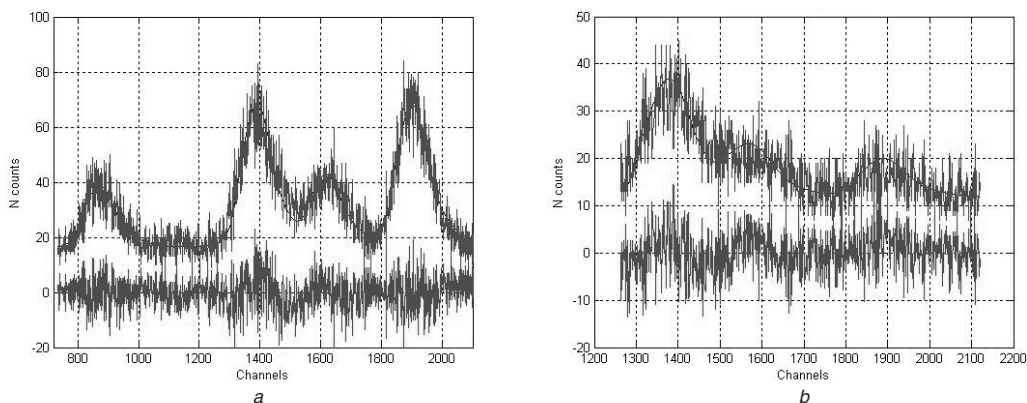


**Fig. 9** Response of the lidar system to the wavy plate

a  $\lambda = 630$  nm  
b  $\lambda = 780$  nm

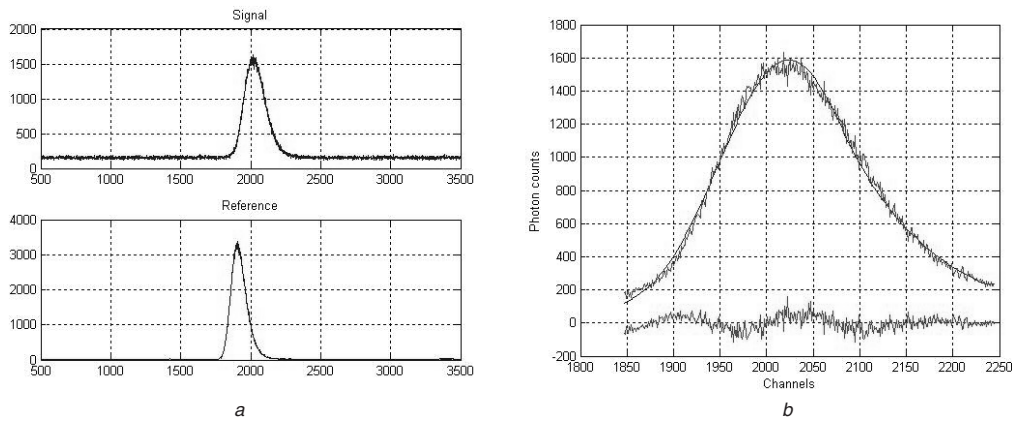


**Fig. 10** *Response of the ladar system to the horn at 630 nm*  
*a* Comparison of the horn response (upper curve) to the corner cube (lower curve)  
*b* Final result for the horn data

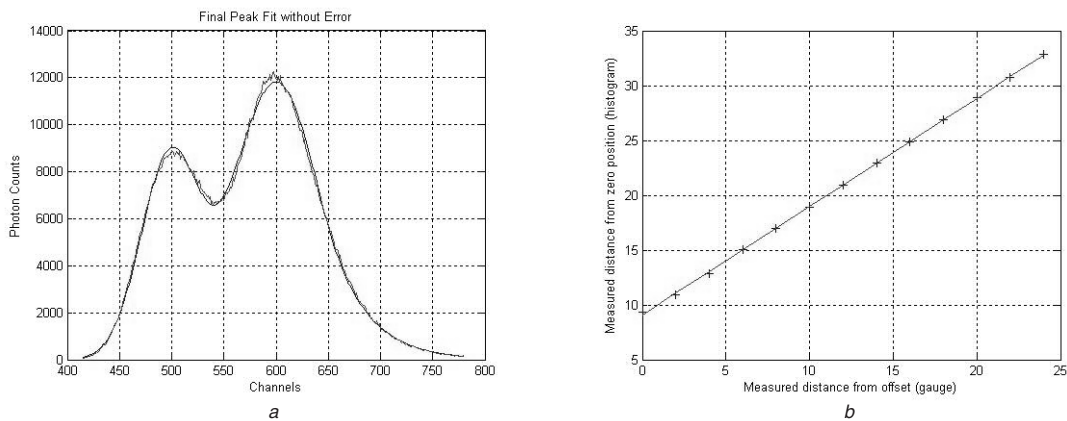


**Fig. 11** *Testing the range resolution using incremental variation of separation of two corner cubes*  
*a* Stand-off distance 330 m, separation 9.3 cm, collection time = 10 s  
*b* Laser measured against gauge-measured separation, for distances from the offset in the range 0–24 cm

to the line is  $y = 9.09 + 0.99x$  (cm), with a mean absolute error of 0.6 mm between the laser and gauge measured data, that is, within the tolerance of the ruled measurement.

## 6 Conclusions and further work

We have developed a multi-spectral ladar system using TCSPC. Here, we have presented the results of a study of the analysis of the photon count data to find the number, positions, amplitudes and shape parameters of the multiple returns in independent channels. The approach we have developed has two stages, first non-parametric bump hunting to find initial estimates of the positions and amplitudes of returns, and second Poisson-MLE of the peak parameters.

We have analysed the behaviour of the algorithm in response to both simulated data, for which the ground truth is known and real data acquired by the multi-spectral system. For the simulated data, we have shown that the bump hunting procedure can locate both modes and co-tangents in the histogram distribution, using diagnostics based primarily on curvature, but we have also considered excess mass. Using curvature as an example, we have computed a decision function based on the difference of Poisson variates, but shown that this differs little from the Gaussian approximation because of the high integrated count rates caused by progressive smoothing. However, we note that the optimum width of the smoothing process is determined by the width of the operating model of the system response.

If unsmoothed data were used, which could be the case for returns of less width on the time axis, the Poisson model should be used, but the error rate would be much higher as the random photon fluctuations would have a greater effect.

The MLE process provides refined estimates that are accurate in determining the positions and amplitudes of the returns, even when the signal-to-background levels are comparable and the returns are closely separated in time. For the simulated data, the use of the correct Poisson-MLE model gives improved estimates of the several signal and background parameters when the photon count rates are low, in agreement with previous work. In general, the mean results from several trials were very close to the simulated values, confirming the accuracy of the approach. For the real targets, we cannot comment on accuracy in the absence of ground truth, and have observed that the problem is ill-posed, as different experimental conditions can result in similar spectra, for example, if the parametric response of the detector changes or the surface is distributed in range, especially where the beam divergence results in a large target footprint. However, our experiments to measure the depth separation of corner cubes for which ground truth is known do show good agreement between the measurements and ground truth.

There are still some additional aspects of the work that merit further investigation. Empirically at least, our experience is that if the reference signal is recent (e.g. acquired concurrently with the target) then one need not vary all the shape parameters of the return if the target is a single,

normal surface. However, one can compensate for a distributed (in distance) surface by varying those shape parameters. Another consideration is whether detailed modelling of the tails is necessary and whether that affects localisation of the peak. On the other hand, such modelling is probably necessary to detect a weak response in the tail of a larger one. Further, we have not really considered the relative merits of employing different information theoretic criteria to make a decision on the number of returns. Finally, we observe that we have not combined the results of the several spectra, either in making a decision about the nature of the return or in making a higher level decision about target identity.

## 7 Acknowledgments

The authors would like to acknowledge the support of Qinetiq Ltd and the Royal Society.

## 8 References

- 1 Amann, M.C., Bosch, T., Lescure, M., Myllyla, R., and Rioux, M.: 'Laser ranging: a critical review of usual techniques for distance measurement', *Opt. Eng.*, 2001, **40**, (1), pp. 10–19
- 2 Baltsavias, E.P.: 'Airborne laser scanning: existing systems and firms and other resources', *ISPRS J. Photogramm. Remote Sens.*, 1999, **54**, pp. 164–198
- 3 Ratches, J.A., Walters, C.P., Buser, G., and Guenther, B.D.: 'Aided and automatic target recognition based upon sensory inputs from image forming systems', *IEEE Trans. Pattern Anal. Mach. Intell.*, 1997, **19**, (9), pp. 1004–1019
- 4 Foy, B.R., McVey, B.D., Petrin, R.R., Tjee, J.J., and Wilson, C.: 'Target characterisation in 3D using infrared LaDAR', *Proc. SPIE*, 2001, **4370**, pp. 181–187
- 5 Churoux, P., Besson, C., and Bouzinac, J.P.: 'Model of a burst imaging LaDAR through the atmosphere', *Proc. SPIE*, 2000, **4035**, pp. 324–331
- 6 Browder, M., Evans, B., Beck, J., Blessinger, M., Blattner, W., LeBlanc, R., and Miles, B.: 'Three dimensional imaging sensors program', *Proc. SPIE*, 2001, **4377**, pp. 73–83
- 7 Johnson, K., Vaidyanathan, M., Xue, S., Tennant, W., Kozlowski, L., Hughes, G., and Smith, D.D.: 'Adaptive LaDAR receiver for multispectral imaging', *Proc. SPIE*, 2001, **4377**, pp. 98–105
- 8 Wallace, A.M., Buller, G.S., and Walker, A.C.: '3D imaging and ranging by time-correlated single photon counting', *Comput. Control Eng. J.*, 2001, **12**, (4), pp. 157–168
- 9 Massa, J.S., Buller, G.S., Walker, A.C., Smith, G.R., Cova, S., Umasuthan, M., and Wallace, A.M.: 'Optical design and evaluation of a three-dimensional imaging and ranging system based on time-correlated single photon counting', *Appl. Opt.*, 2002, **41**, (6), pp. 1063–1070
- 10 Pellegrini, S., Buller, G.S., Smith, J.M., Wallace, A.M., and Cova, S.: 'Laser based distance measurement using picosecond resolution time-correlated single photon counting', *Meas. Sci. Technol.*, 2000, **11**, pp. 712–716
- 11 Umasuthan, M., Wallace, A.M., Massa, J.S., Buller, G.S., and Walker, A.C.: 'Processing time-correlated single photon data to acquire range images', *IEE Proc., Vis. Image Signal Process.*, 1998, **145**, (4), pp. 237–243
- 12 Rasiah, A.I., Togneri, R., and Attikiouzel, Y.: 'Modelling 1D signals using Hermite basis functions', *IEE Proc., Vis. Image Signal Process.*, 1997, **144**, (6), pp. 345–354
- 13 Stellari, F., Zappa, F., Cova, S., Porta, C., and Tsang, J.C.: 'High-speed CMOS circuit testing by 50 ps time-resolved luminescence measurements', *IEEE Trans. Electron Devices*, 2001, **48**, (12), pp. 2830–2834
- 14 Harezlak, J.: 'Bump hunting in regression data revisited'. MPhil thesis, Simon Fraser University, British Columbia, 1998
- 15 Haldane, J.B.S.: 'Simple tests for bimodality and bitangentiality', *Ann. Eugen.*, 1952, **16**, pp. 359–364
- 16 Silverman, B.W.: 'Using kernel density estimates to investigate multimodality', *J. R. Stat. Soc.*, 1981, **43**, pp. 97–99
- 17 Chaudhuri, P., and Marron, J.S.: 'SiZer for exploration of structure in curves', *J. Am. Stat. Assoc.*, 1999, **94**, (447), pp. 807–823
- 18 Fisher, N.I., and Marron, J.S.: 'Mode testing via the excess mass estimate', *Biometrika*, 2001, **88**, (2), pp. 499–517
- 19 Skellam, J.G.: 'The frequency distribution of the difference between two Poisson variates belonging to different populations', *J. R. Stat. Soc. Ser. A*, 1946, **109**, p. 206
- 20 McLachlan, G., and Peel, D.: 'Finite mixture models' (Wiley, 2000)
- 21 Hannam, M.D., and Thompson, W.J.: 'Estimating small signals by using maximum likelihood and Poisson statistics', *Nucl. Instrum. Methods Phys. Res. A*, 1999, **431**, pp. 239–251
- 22 Hauschild, T., and Jentschel, M.: 'Comparison of maximum likelihood estimation and chi-square statistics applied to counting experiments', *Nucl. Instrum. Methods Phys. Res. A*, 2001, **457**, pp. 384–401
- 23 Stoneking, M.R., and Den Hartog, D.J.: 'Maximum-likelihood fitting of data dominated by Poisson statistical uncertainties', *Rev. Sci. Instrum.*, 1997, **68**, (1), pp. 914–917
- 24 Burnham, K.P., and Anderson, D.: 'Model selection and multi-model inference' (Springer-Verlag, 2002)
- 25 Lawson, C.L., and Hanson, B.J.: 'Solving least squares problems' (Prentice-Hall, Englewood Cliffs, NJ, 1974)